RESEARCH ARTICLE

Journal
American Ceramic Society

Impact of MgCl$_2$ on the mechanical properties of alite pastes at mesoscale and nanoscale

Yanjie Sun[1] | **Yong Tao**[1] | **Roland J. M. Pellenq**[2] | **Chi Sun Poon**[1]

[1]Department of Civil and Environmental Engineering, The Hong Kong Polytechnic University, Hung Hom, Kowloon, Hong Kong

[2]Institut Européen des Membranes, CNRS and Université of Montpellier, Montpellier, France

Correspondence
Roland J. M. Pellenq, Institut Européen des Membranes, CNRS and Université of Montpellier, Montpellier, France.
Email: roland.pellenq@cnrs.fr

Chi Sun Poon, Department of Civil and Environmental Engineering, The Hong Kong Polytechnic University, Hung Hom, Kowloon, Hong Kong.
Email: cecspoon@polyu.edu.hk

Abstract
While the MgCl$_2$ mixing alite paste causes degradation of the modulus and hardness of C−S−H formed, the underlying degradation mechanism needs to be better understood. This study comprehensively analyzed the mechanical properties of alite pastes mixed with MgCl$_2$ solutions, examining the effects at both mesoscale and nanoscale. The in situ X-ray diffraction analysis revealed that the formation of brucite occurred at a very early age together with the formation of portlandite, which may induce a loosened packing density of C−S−H and served as the primary cause of modulus and hardness degradation. We used Bayesian statistical models to fit the nanoindentation data of C−S−H. By extrapolation at a packing fraction equal to unity, we were able to extract elastic properties (modulus and hardness) of the C−S−H nanograins. The nanoscale C−S−H elastic modulus showed no significant alterations in the mechanical properties of the C−S−H nanostructures. Atomistic simulations also suggested that Mg^{2+} ions preferably substitute interlayer Ca rather than intralayer Ca in C−S−H, and the Mg docking in CSH induced a very modest volume contraction.

KEYWORDS
alite, atomistic simulation, degradation, MgCl$_2$, nanoindentation

1 | INTRODUCTION

Seawater concrete has drawn more and more attention due to the freshwater shortage problem, especially in regions like the Middle East, North Africa, and some remote islands.[1,2] By 2030, about 700 million people are predicted to suffer water scarcity, according to a World Meteorological Organization (WMO) report.[3] In contrast, about 71% of the surface of the Earth is covered with seawater. That is a vast water resource.

The early application of seawater concrete can be traced back to ancient Roman concrete more than 2000 years

ago.[4] The structures still showed excellent longevity. However, modern concrete structures rarely use or forbid seawater in concrete mixing. The high chloride content in seawater causes the steel bars, the main component in concrete, to get rusted.[5–7] Fortunately, the invention and application of fiber-reinforced polymer (FRP) may support promising seawater usage since FRP bars show excellent corrosion resistance and better durability when exposed to seawater.[8,9]

Significant progress has been made in recent years in the study of seawater concrete, with research focusing on cement hydration,[10–15] microstructure[10,12–15] and

---

mechanical strength.[10,12–15] Most studies agreed that seawater concrete attains higher early strength than freshwater concrete.[10,16–18] Moreover, incorporating seawater would cause the morphology change of hydration products. The main morphological change observed was in the C−S−H structure. In contrast to the isolated clusters observed in distilled water, the C−S−H formed in seawater-mixed samples exhibited dense clusters interconnected with needle-like gypsum crystals.[19] However, there are inconsistent research results regarding the mechanical performance of seawater concrete. For instance, Younis et al. showed that with the incorporation of seawater as the mixing water, the compressive strength of seawater concrete is inferior to ordinary concrete after 28 days (decreased about 7%−10%),[10] which was probably due to leaching of hydration products,[20] or sulfate attack.[21] While Shi et al. found that the 28 days compressive strength of seawater concrete was 22% larger than that of ordinary freshwater concrete, attributed to the acceleration effect of seawater and more C−S−H formed.[22] This discrepancy may be due to differences in seawater and cement types.

Seawater is a complicated system, abundant with various ions, mainly Na^+, Mg^{2+}, and Cl. So, some research has been conducted on single-salt solutions. There were already some studies on the effects of NaCl on the hydration of cement[23] and alite.[24–26] Similar to seawater, an acceleration effect was also observed. However, when it comes to the impacts of the $MgCl_2$ solution and seawater, degradation was observed for the alite pastes despite the acceleration effect, as indicated by our previous study.[24] Effects of different cations based on their chloride salts were studied, and the results showed that incorporating Mg^{2+} would decrease the micro-mechanical properties (modulus and hardness) of alite pastes.[27] Nevertheless, the impact of Mg^{2+} incorporation on the mechanical properties of C−S−H itself at the micro level, excluding the mesopores among the gels, remains unexplored. Several studies have suggested that Mg^{2+} may enter the C−S−H structure.[28,29] A recent study by Liu et al. has combined multiple techniques to demonstrate that a small amount of Mg^{2+} would incorporate into the interlayer of C−S−H without affecting the structure of C−S−H.[30] Also, an extension model for the uptake of alkaline earth metals by C−S−H indicated magnesium uptake by C−S−H, but the amount was limited.[31] However, in the previous study, the effect of Mg^{2+} on the nanotexture and mechanical properties of C−S−H is still to be understood from the nanoscale using the atomistic simulation technique and experimental analysis.

Nanoindentation has emerged as a valuable technique for investigating the micromechanical properties of cementitious materials.[32] This method involves the application of controlled forces on a small scale, allowing for the determination of crucial parameters such as modulus and hardness. These parameters are essential for comparing the properties of hydration products, and their accurate measurement aids in understanding the mechanical behavior of cementitious materials.[33] In addition to nanoindentation, atomistic simulations offer another effective approach for studying the underlying mechanisms governing various mechanical behaviors observed in cementitious materials. By simulating the interactions between individual atoms, atomistic simulations contribute to unraveling the complex nature of hydration products and their mechanical response.[34,35]

By combining various experimental techniques with atomistic simulations, this study aimed to comprehend the impact of $MgCl_2$ on the mechanical properties of alite pastes at both the mesoscale and nanoscale. Through this understanding, we hope to improve the application of seawater concrete and enable the design of its mix more scientifically.

2 | MATERIALS AND METHODS

2.1 | Materials and sample preparation

Laboratory-synthesized alite was used in this study, and the synthesis process followed the method proposed by Li et al.[36] Based on the X-ray diffraction (XRD) analysis, the purity of the raw material reached 94.1 wt.%. Malvern MS3000 laser particle analyzer was adopted to analyze the particle size distribution. The average particle size and specific surface area of the alite powders were 16.9 μm and 7 202 cm^2/g, respectively. The details of the properties of alite can be checked in our previous studies.[27]

0.42 mol/L $MgCl_2$ (MC) solutions were prepared with AR-grade reagent. The alite was mixed separately with DI water and MC solution at a solution-to-binder ratio of 0.5.

2.2 | Characterization and analysis methods

In situ XRD was performed using a Rigaku Smartlab diffractometer. The power generator operated at 45 kV and 200 mA. Cu Kα radiation was used. Alite was mixed with aimed solutions at the solution to the binder of 0.5 for 1 min, then placed on the sample holder. The samples were covered with Kapton polyimide film to minimize water loss and carbonation effects. During the in situ XRD test, the data were recorded every 50 min, up to 500 min. The test range was from 5° to 80° 2θ with a step width of 0.02° 2θ. The Rietveld refinement was conducted on the softwater Highscore Plus 4.9, and the external K-factor
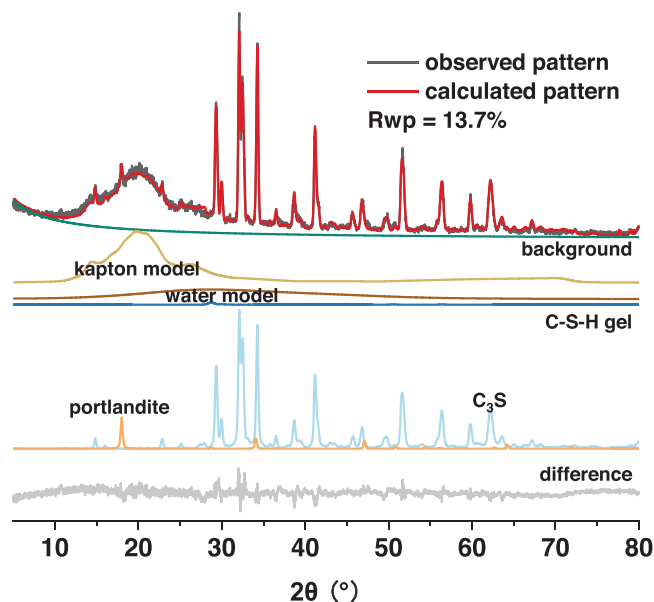
FIGURE 1 In-situ XRD pattern of hydrating alite paste after 500 min hydration. The pattern of each profile is shown. Rwp refers to the weighted residue, where a lower value indicates a better fitting. XRD, X-ray diffraction.

corrected method was selected.[37] ZnO was adopted as the external standard to help modify the *K*-factor. The Kapton film model was obtained with a Pawley fit with a ZnO sample covered with Kapton film.[38] Using a similar approach, a water/ZnO ratio of 0.5 sample was used to determine the water model and a 24 h hydrated alite paste was used to determine the C–S–H model. The example for the quantification analysis is shown in Figure 1, where the contents of alite and portlandite of the pastes can be determined.

The micro-mechanical properties of the alite pastes were analyzed with a Nano-indenter (Hysitron TI Premier, Bruker) equipped with a three-sided pyramid Berkovich tip. Before the testing, the equipment was calibrated on a standard sample, fused quartz. The maximum loading of 2 000 µN was applied on the polished surface of the alite pastes. One hundred data points were collected for statistical analysis based on each sample's multivariate cluster modeling approach. The maximum likelihood estimation[39] was adopted, assuming the data followed a Gaussian mixture model. The nanoindentation results were further analyzed to get the packing density based on the method proposed by Ulm et al.[40,41] For detailed information on the nanoindentation test, we refer to a previous research publication.[27]

The structure of C–S–H was studied based on the ^{29}Si solid-state nuclear magnetic resonance (NMR) spectrometer (JEOL ECZ 500MHZ). One thousand twenty-four scans were conducted for each test, and the relaxation delay was

20 s. The spectra were then deconvoluted to differentiate various Si statuses.

2.3 | Atomistic simulation methods

2.3.1 | C–S–H model

To describe the disordered molecular structure of C–S–H, Pellenq et al.[34] proposed a realistic model for C–S–H with the stoichiometry of $(CaO)_{1.65}(SiO_2)(H_2O)_{1.73}$. The C–S–H model was generated by introducing defects in an 11 Å tobermorite configuration, following a combinatorial procedure. 11 Å tobermorite consists of pseudo-octahedral calcium oxide sheets surrounded by tetrahedral silicate chains. The latter consists of bridging oxygen atoms and Q^2 silicon atoms (having two bridging and two non-bridging terminal oxygen atoms). Those negatively charged calcium–silicate sheets are separated by an interlayer spacing, which contains water molecules and charge-balancing calcium cations.[42] Whereas the Ca/Si ratio in 11 Å tobermorite is 1, this ratio is increased to 1.7 in the present C–S–H model by randomly removing electroneutral SiO_2 groups. Defects in silicate chains provide possible sites for the adsorption of extra water molecules. The adsorption of water molecules in the structurally defective tobermorite model was performed via the Grand Canonical Monte Carlo method, ensuring equilibrium with bulk water at constant volume and room temperature.[43] A comprehensive study covering the range of Ca/Si ratio relevant to C–S–H chemistry (i.e., between 1 and 2) was subsequently carried out by Qomi et al.[35,44–46] using reactive interatomic potentials allowing to take care of reactivity induced by the numerical sample preparation procedure. When we construct the molecular models for C–S–H, we may inevitably cause some defects (e.g., poorly coordinated structure of surface ions), which might influence the surface stability (reactivity). Therefore, as conducted in previous studies, we used the reactive interatomic potentials to equilibrate the models by allowing the chemical bonds to form or break. It was shown that the used sample here at Ca/Si = 1.7 did not show any significant change besides local relaxation and the breakage of a few water molecules. This was subsequently confirmed using ab initio density-functional theory (DFT) calculations[47] (see SI for DFT pair correlation functions).

2.3.2 | Exchanging calcium for magnesium

In the context of this work, our atomistic simulation initiative is mainly inspired by nanoindentation experiments. The experimental results indicate that Mg ions have a

significant impact on the modulus of C–S–H. However, it cannot be determined whether Mg ions alter the modulus of C–S–H by entering the molecular structure of C–S–H itself. Therefore, we considered using atomic simulations to calculate the hypothetical impact of Mg ions entering C–S–H on the modulus directly. We explored the possible set of substitutions, including both interlayer and intralayer calcium sites in the C–S–H structures, provided that electro-neutrality is maintained: Ca and Mg share the same +2 electric charge, Mg being, however, a smaller species than Ca (Mg–O bond length in MgO is equal to 2.05 Å, while Ca–O bond length in CaO is equal to 2.40 Å, see SI). Still, it remains unclear from NMR experiments how interlayer Mg can be accommodated in silica chain vacancies or lacunes, as these are tetrahedral coordination sites incompatible with magnesium chemistry. Somehow the same question holds for intralayer sites of the pseudo-octahedral symmetry, again not a priori compatible with magnesium chemistry in oxide phases (MgO and CaO being cubic crystals). In the second stage, the influence of magnesium substitutions on the mechanical properties of Mg–C–S–H composite materials will be assessed.

2.3.3 | Interatomic potentials

Modeling and simulating complex hydrated oxides require a well-defined and carefully characterized energy model that can simultaneously reproduce their mechanical properties and structural configurations. In our C–S–H structure, there are different chemical environments for the same elements, we need to combine different potential functions to describe the interactions between atoms in the C–S–H model. Different types of atoms and a diverse bonding environment for a certain atom shadow the transferability of candidate potentials. For instance, oxygen atoms can be either in silica chains, octahedral calcium sheets or water molecules, exhibiting different behaviors in each chemical environment. It is covalently bonded in silica chains, interacts with different species of calcium atoms in an ionic-covalent fashion and constructs water molecules with hydrogen atoms. The force field method describes the interaction between different species by grouping common interatomic potentials. The force field employed in this study uses a combination of Lennard–Jones, Buckingham, Morse, Coulombic, and three-body terms to construct the potential energy. The calculation of electrostatic interactions between pairs of ions is carried out using the 3D-Ewald summation method. The core–shell model is applied to reproduce the polarizability of oxygen atoms in the structure effectively.[34,48] The anion oxygen atoms in the layers and water molecules are modeled as polarizable entities consisting of a core and a shell

linked via an elastic spring. The transferability of this force field has been checked against numerous experimental data and quantum-mechanical calculations regarding the Ca, Mg, Si, O, OH/H_2O system.[48,49] More specifically, the transferability of geometrical and mechanical properties was checked for brucite, $Mg(OH)_2$[49] and Lizardite (Mg-containing silicate mineral[50]). All potential expressions and parameters are given in the Supporting information of this work, along with results for the mentioned series of Mg-containing crystalline solids. Note that the core–shell potential approach gives reasonable results for both textural and elastic properties. In this work, we used the GULP simulation code[48] to perform free energy minimization at room temperature using the Hessian diagonalization approach, as outlined in the Supporting information.

3 | RESULTS AND DISCUSSION

3.1 | Mesoscale analysis

The experimental results for the nanoindentation test are shown in Figure S1. It showed that there were still some data in the range of over 40 GPa, indicating some anhydrous alite. It meant that even though at 90 d, more alite was hydrated in the MC system. However, the amount was limited. For both systems, the hydration degree was very high, and most phases were hydration products.

For the C–S–H, it can be further divided into three phases (pores/defects, low-density (LD) C–S–H and high-density (HD) C–S–H).[51] The deconvolution results are shown in Figure 2. The results indicated that the modulus and hardness of all three phases decreased when alite was mixed with MC solution compared to the DI system. In the case of pores/defects, the modulus decreased from 8.45 ± 0.43 GPa for the DI system to 5.17 ± 1.19 GPa for the MC system, while the hardness decreased from 0.18 ± 0.03 to 0.08 ± 0.07 GPa. Similar tendencies were observed for the properties of LD C–S–H and HD C–S–H. These results indicated a degradation in the hydration products, consistent with our previous study.[27]

The packing densities were calculated based on the method proposed by Ulm et al.,[40,41] the sample was considered as a porous material consisting of two components: a cohesive and frictional solid phase with a packing density, and an empty pore space, which can be calculated as 1—packing density. The packing density can be correlated with the Er and H by the following equations:

$$\frac{Er}{m_s} = \Pi_M \left(v_s, \eta, \eta_0 \right)$$

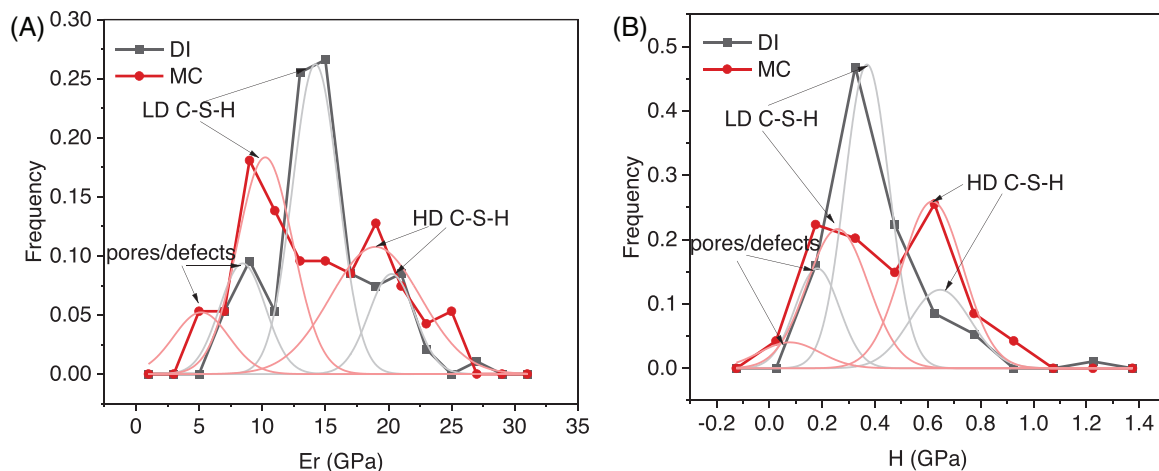$$\frac{H}{c_s} = \Pi_H \left(\alpha_s, \eta, \eta_0, \theta \right)$$

FIGURE 2 Deconvolution results of (A) modulus and (B) hardness of alite pastes mixed with DI and MC solutions and cured for 90 days.
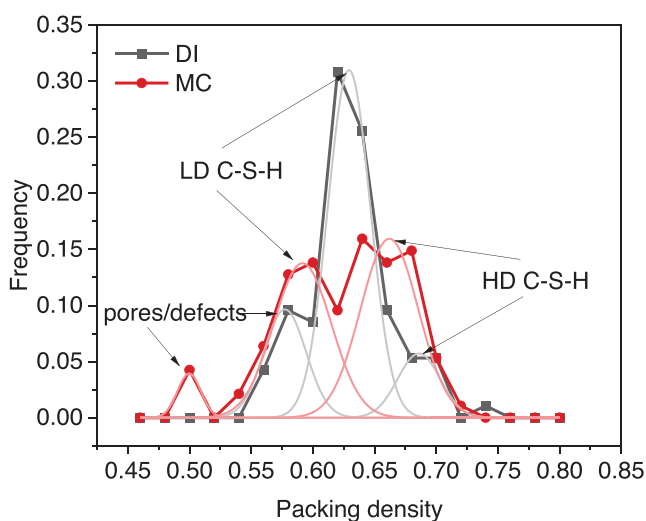

FIGURE 3 The packing density distribution of alite pastes.

where m_s indicates the modulus when packing density (η) is close to 1, v_s is Poisson's ratio, cohesion is represented by c_s, the friction coefficient is α_s, and η_0 is the solid percolation threshold. With a hundred testing points, an inverse fitting was applied to fit each parameter. The packing density results were plotted in Figure 3. There were more weak pores/defects for the MC system, and the packing density was 0.50 ± 0.01, while the value for the DI system was 0.58 ± 0.01. The packing density for LD C–S–H also decreased from 0.63 ± 0.01 to 0.59 ± 0.01 when the alite was mixed with DI and MC solutions. For the HD C–S–H, the packing density for the DI system was 0.69 ± 0.01, while the value for the MC system was 0.66 ± 0.01.

In order to study the phase evolution at the early hydration, an in situ XRD test was conducted, and the representative patterns are shown in Figure 4. At 150 min, there was already a peak of the brucite formation. It indicated the early formation of brucite. That was consistent

with our previous simulation and experimental results.[24] There was already a peak for portlandite at 200 min in the MC system. It was consistent that the incorporation of MC would accelerate the hydration rate. At 400 min, the peak for brucite became more evident. Even though portlandite was formed in the DI system, the content was far less than in the MC system. The in situ XRD results were further quantified and summarized in Figure 5. The consumption of alite was an index for the hydration degree. It was found that before 150 min, the consumption of alite was limited for both groups. It was because they were in their induction period. Afterward, the consumption rate started to show a difference. At 500 min, about 53% of the total alite was consumed, much higher than in the DI system. Another critical phase in alite hydration was portlandite. The formation of portlandite was faster in the MC system than in the reference system. At 500 min, the portlandite content formed in the MC system was over four times the value in the DI system. That was mainly due to the increase in the ionic strength of the solution so that the dissolution of alite and calcium concentration increased.[24] Even though the incorporation of MC accelerated the hydration process of alite at an early age, the faster hydration may lead to faster desaturation of the large pores, which would hinder the growth of hydration products. That can be another possible reason for the modulus and hardness degradation of C–S–H.[52]

3.2 | Microscale analysis

In this work, we used atomistic simulations to explore the ability of C–S–H to dock magnesium ions in substitutions for calcium ones. As described in Section 2.3.2, considering the structural characteristics of C–S–H and the coordination structures of Mg^{2+} and Ca^{2+} ions, Mg ions can enter
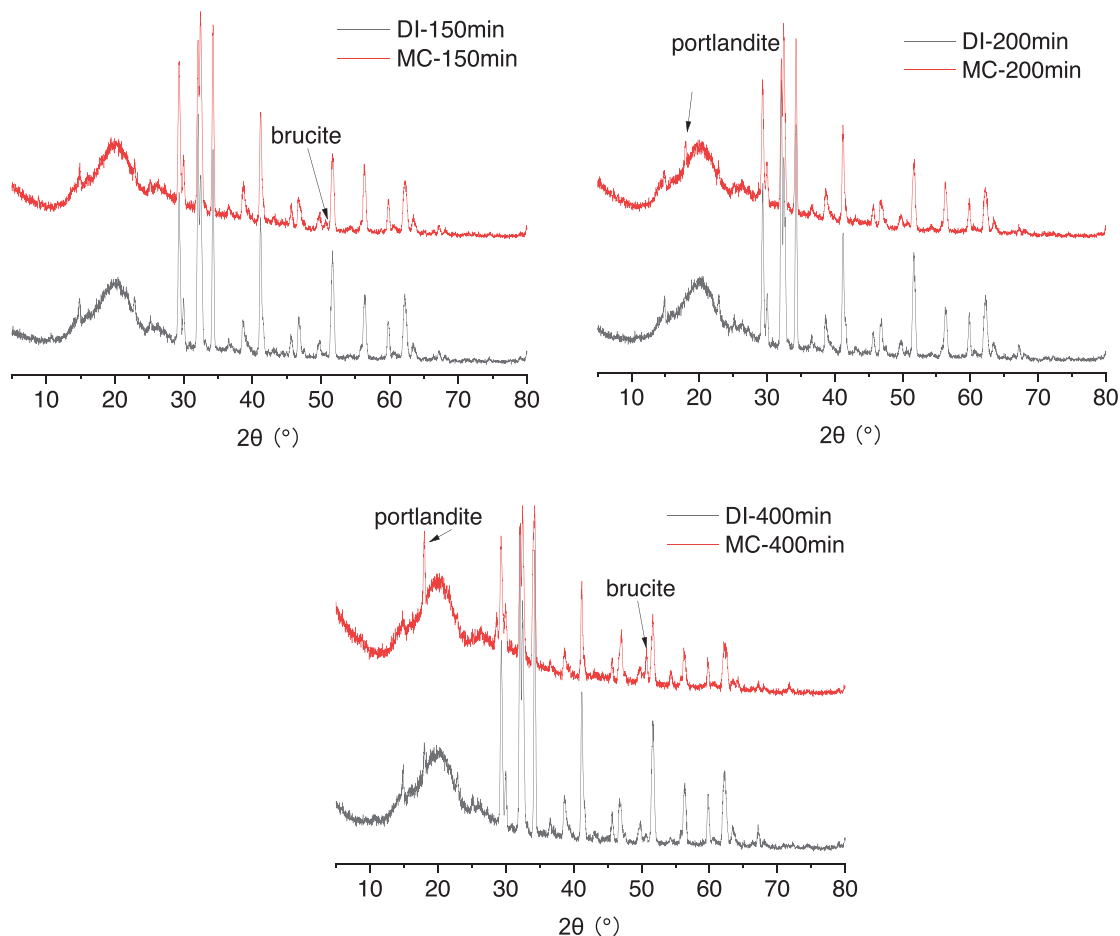
FIGURE 4 Selected in situ XRD patterns of alite mixed with DI water and MC solutions, hydrated for 150, 200, and 400 min. XRD, X-ray diffraction.
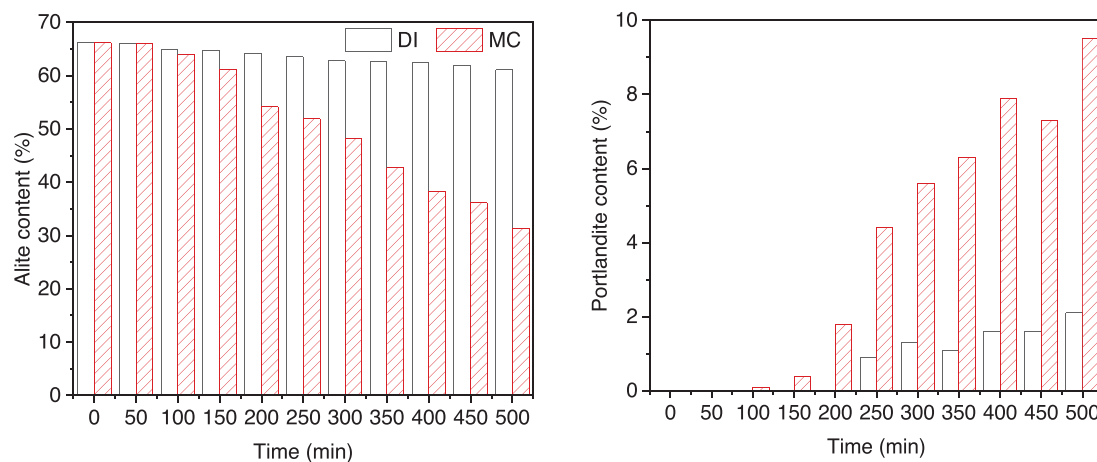

FIGURE 5 Quantification results for the variation of alite and portlandite content.

the interior of C–S–H in two possible ways: by substituting Ca^{2+} ions within or between the layers. Figure 6 shows the energy changes of the system when Mg^{2+} replaces Ca^{2+} ions in these two positions separately. Focusing on inter-

layer substitutions only (see Figure S2), from one to two $Mg^{2+} \rightarrow Ca^{2+}$ levels of substitutions lead to a decrease of energy by about a maximum of 3–4 eV/ Mg^{2+}. Due to the smaller radius of Mg^{2+} ions than Ca^{2+} ions, when Mg^{2+}
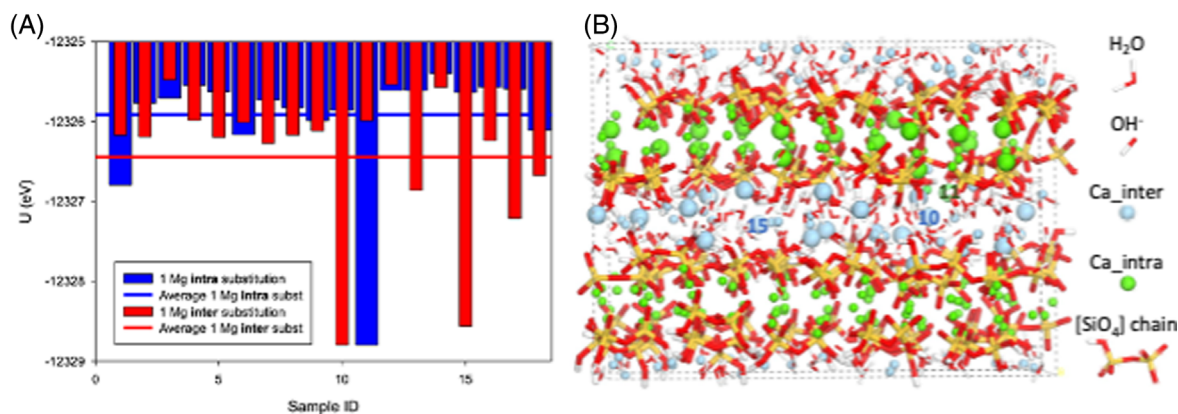
FIGURE 6 (A) Potential energy change upon 1 Mg^{2+} → 1 Ca^{2+} substitution(s) for both inter- and intra-layer Ca sites. (B) The C–S–H model showing the different inter- and intra-layer Ca sites that are substituted by Mg ions. The substituted Ca atoms are magnified and the peculiar Ca sites with significantly lower potential energies are labeled for clarity.

replaces Ca^{2+}, the newly formed Mg–O bonds are shorter than Ca–O bonds. The Mg–O interactions are stronger than the Ca–O interactions, resulting in a greater release of energy and a lower total energy of the system. It is consistent with the fact that Mg^{2+} size is smaller than that of Ca^{2+}, leading to a larger contribution of the electrostatic interaction.

In general, interlayer substitutions stabilize the system more than intralayer ones since the former results in lower potential energy on average. However, it is worth noting that there are some peculiar inter- and intra- layer Ca sites (e.g., Nos. 10, 11, 15) featuring significantly lower potential energy after the Mg substitution. It is understandable based on the structure model in Figure 6B. As mentioned above, the decrease in potential energy is due to the newly formed Mg–O interactions is stronger than the original Ca–O interactions. Therefore, the weaker the original Ca–O bonds, the lower the potential energy after the Mg substitution. Compared with most inter-layer Ca sites possessing stronger interactions with the silicate chains, sites 10 and 15 exhibit weaker Ca–O bonds with water and OH– ions. Similarly, the intra-layer Ca site 11 is almost in the inter-layer region due to the defective porous nature of the C–S–H network, where the Ca–O interactions are much weaker than that of Ca sites in the intra-layer region.[53] Thus, the Mg substitution energy of site 11 is apparently lower than the other intra-layer Ca sites.

To analyze the C–S–H texture closely upon Mg exchange (inter- and intra-sites), we calculated the Mg–O (solid) and the Mg–O (water) pair correlation functions as shown in Figure S4. The Mg–O (solid) distance in the C–S–H model shows a first correlation peak at 2.05 Å, fairly close to that found in brucite (with the same Mg–O potential: 2.12 Å), contrasting with the Mg–O (water) at 2.75 Å. Figure 7 shows that in either case (intra- or inter-layer

substitution sites), Young's modulus for one substitution remains relatively constant and close to that of the pristine C–S–H structure (65 GPa).

Figure 8 presents the variation of the averaged interlayer distance as a function of the level of interlayer substitutions. The systems tend to have a steady but modest shrinkage from Mg/(Mg+Ca) > 0.01 upon increasing substitutions. When the Mg substitution level is less than 10%, the interlayer spacing does not show significant changes (−0.5% to +0.5% range). However, when the Mg substitution level exceeds 10%, the interlayer spacing gradually decreases with increasing Mg substitution. This is because the difference in ionic radii (Mg^{2+} ions have a smaller radius than Ca^{2+} ions) leads to an accumulating contraction between the layers, which becomes more pronounced over time. The Mg content reflects on Young's modulus of the Mg–C–S–H systems (Figure 9). As expected in the swelling domain (Mg/(Mg+Ca) < 0.12), it was observed a decrease in Young's modulus while in the shrinkage domain, an increase of Young's modulus is obtained, which is in agreement with the expected behavior of Young's modulus of materials with increasing density.[54] This induced modulus increase by Mg substitution has also been observed in calcium sulfoaluminate hydrates.[55,56] It was noted that below the swelling–shrinkage threshold transition, the Young's modulus of Mg–C–S–H's tends to be lower than that of the pristine structure while above (i.e., at larger Mg content), the Young's modus of C–S–H's tends to be larger than that of the initial model. This overall impact of the Mg intake in C–S–H is also reflected in Figure 10, which shows that Young's modulus in the shrinkage domain is generally above the value of the pristine C–S–H (with an interlayer spacing at 12 A) by contrast to that obtained in the swelling regime that corresponds to Young's modulus values lower than that of the initial C–S–H structure. Overall, low values of the Mg/(Mg+Ca)

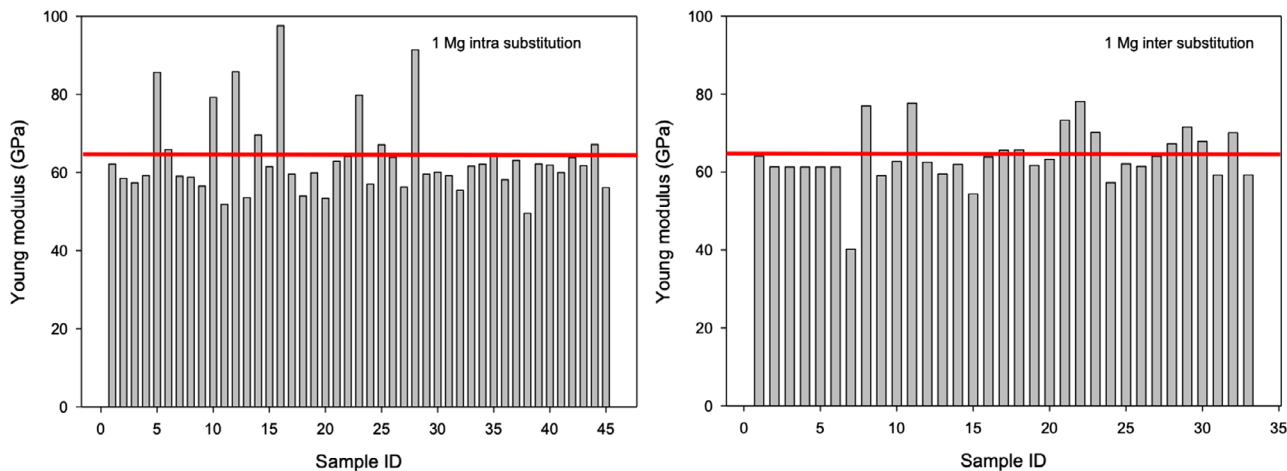**FIGURE 7** Variations for the Young's modulus for 1 $Mg^{2+} \rightarrow Ca^{2+}$ substitution in intra- and inter-layer sites.
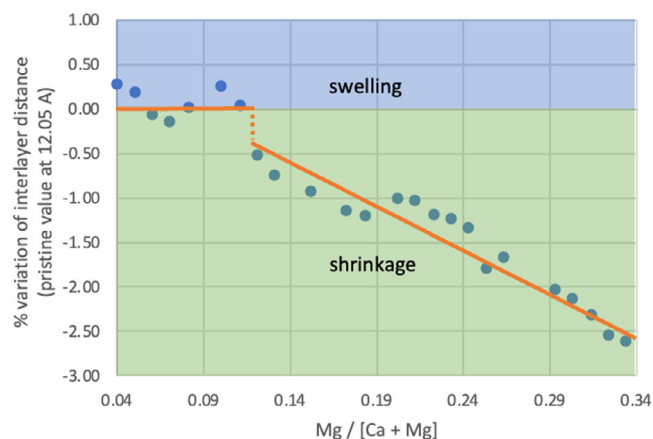
FIGURE 8 The variation of the interlayer distance upon $Mg^{2+} \rightarrow Ca^{2+}$ inter-layer substitutions.

ratio (less than 12%) tend to induce a modest swelling of the Mg–C–S–H structures with a significant decrease of the Young's modulus, while a larger Mg/(Mg+Ca) ratio is prone to induce shrinkage and an increase of the Young's modulus of the Mg–C–S–H's.

To compare the simulation with the experiment, the modulus and hardness of alite pastes were modeled to a density close to 1 (Figure 11). A similar indentation modulus occurred when the packing density came to 1. Even higher indentation hardness for the MC group when packing density comes to 1. For DI samples, the stiffness was 60.003 GPa, which was quite similar to the value for the MC group (60.189 GPa). As for the cohesion, the value increased from 0.256 to 0.289 GPa, as $MgCl_2$ was incorporated. The obtained results differed from the predictions of the atomistic simulation, which suggested that a limited substitution of Mg would lead to a decrease in the modulus of C–S–H. Consequently, we aimed to address this inconsistency through a discussion. While some literature suggested the possibility of Mg^{2+} incorporation into the C–S–H structure,[29] the amount seemed to be very low or can be ignored. That was also indicated by Bernard et al., who emphasized the lack of direct experimental evidence for Mg uptake by C–S–H.[57] Therefore, based on the results above, it can be concluded that such incorporation would not result in the degradation of the C–S–H gel.

The spectra of the NMR and deconvolution results are shown in Figure 12 and Table 1 separately. The deconvolution method was a combination of Lorentzian and Gaussian functions. The status of the SiO_4 tetrahedron was classified by Q^n, where n referred to the number of bridging oxygen of the tetrahedron.[58] Overlapped Q^0 species were deconvoluted to three different peaks, representing the unhydrated alite phase.[59,60] Compared to the DI group, the positions of these peaks did not vary much. However, the integration of Q^0 for the MC group was 11.6 %, lower than the value for the DI group (18.2%). That indicated more alite was hydrated for the MC group. Q^1 and Q^2 species represented the tetrahedrons at the end and the middle of the C–S–H chains.[61] The positions of these two peaks (Q^1 and Q^2) did not vary much between these two groups. That indicated that the structure of C–S–H did not vary much with the incorporation of MC. As shown in Table 1, the MC mixed alite paste was richer in Q^1 species. That meant the C–S–H formed in the MC system had more end-chain tetrahedra, which indicated a shorter mean chain length (MCL) and lower polymerization degree (PD) of C–S–H. These two parameters were calculated as $MCL = 2 \times (Q^1 + Q^2)/Q^1$ and $PD = Q^2/Q^1$.[24] The breaking of C–S–H chains caused a decrease in MCL and PD, which may be due to more cations (Ca^{2+} and Mg^{2+}) to break the network of silicate chains.[24,62] The existence of Mg^{2+} might be incorporated into the gap of the SiO_4 tetrahedron.[29] However, the effect was limited. Also,
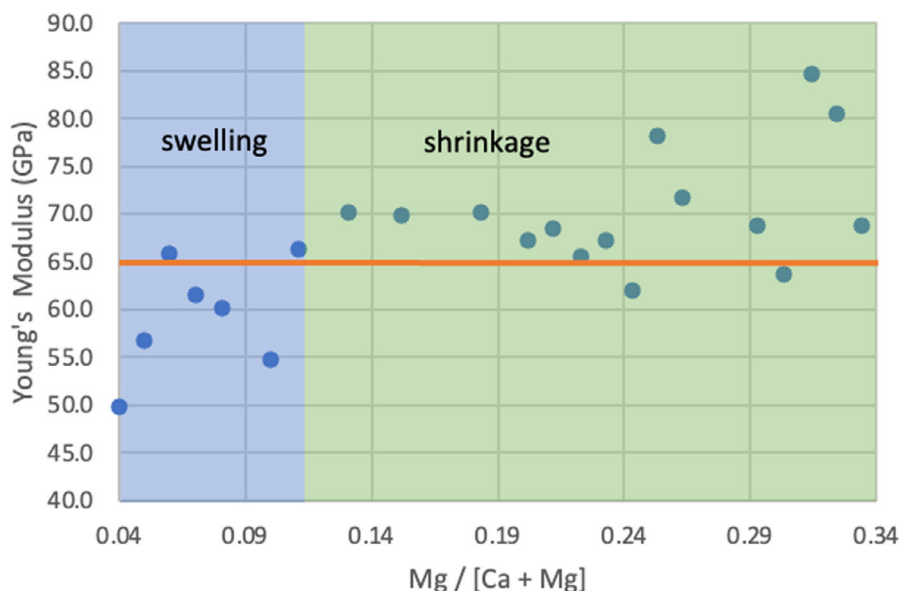
FIGURE 9 Young's modulus as a function of the level of $Mg^{2+} \rightarrow Ca^{2+}$ substitutions.

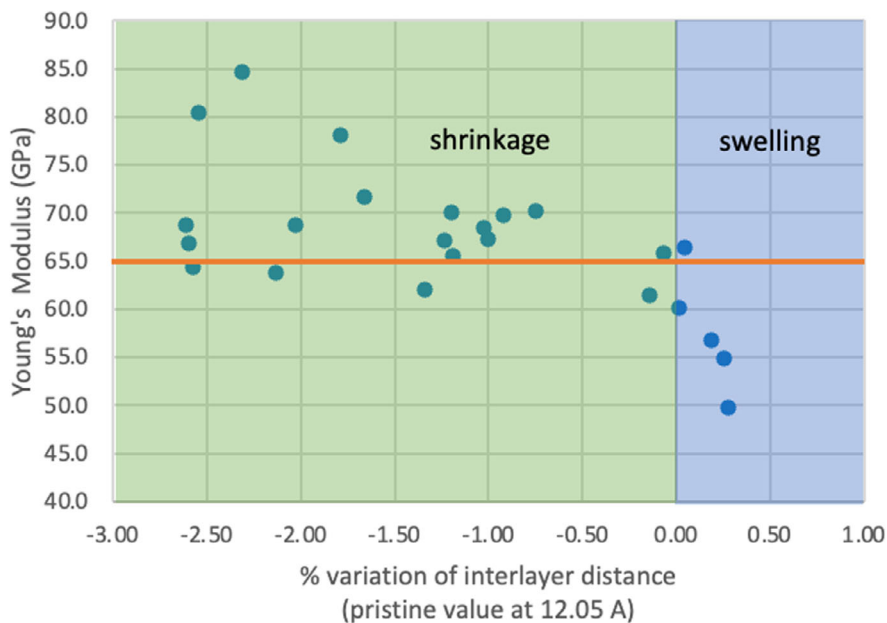**FIGURE 10** Variation of the Young's modulus as the systems evolves from shrinking to swelling upon $Mg^{2+} \rightarrow Ca^{2+}$ substitutions.

TABLE 1 Deconvolution results of the ^{29}Si MAS NMR spectra for the samples.

Samples	δ (^{29}Si) (ppm) and integration (%)					MCL	PD (%)
	Q^0-1	Q^0-2	Q^0-3	Q^1	Q^2		
DI	−68.9 (2.0)	−71.3 (6.4)	−73.6 (9.8)	−79.2 (58.6)	−84.7 (23.2)	2.79	39.5
MC	−68.9 (0.6)	−71.6 (4.7)	−73.8 (6.3)	−79.0 (64.0)	−84.8 (24.4)	2.76	38.2

atomistic simulations reveal that incorporating Mg^{2+} in the C–S–H structure does not affect the micro-mechanical properties. So, the changes in the C–S–H induced by Mg^{2+} upon Ca^{2+} substitutions at the nanoscale are not the main reason for the observed degradation. Based on the nanoindentation analysis, the degradation was due to the decrease in the packing density induced by the early formation of brucite. Since the micro-mechanical
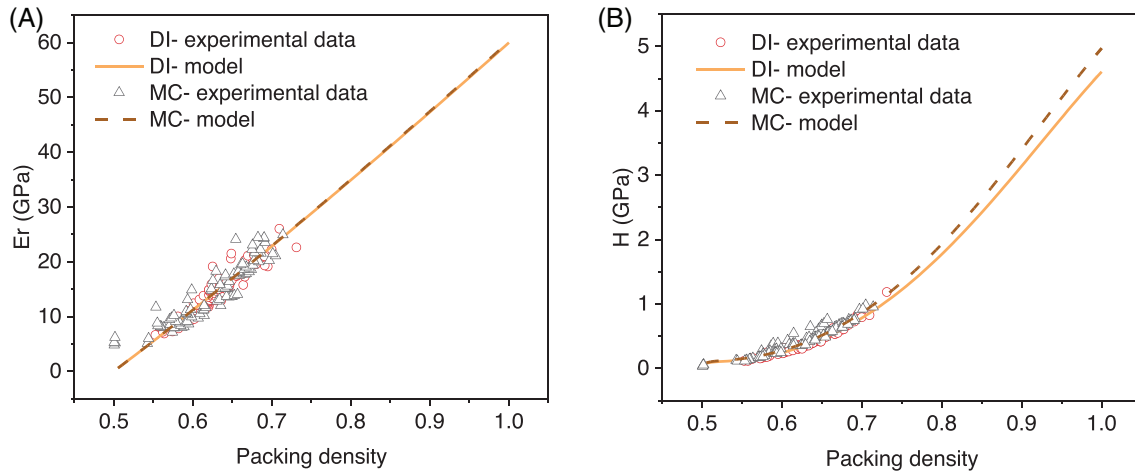
FIGURE 11 The relationship between micro-mechanical properties and packing density.
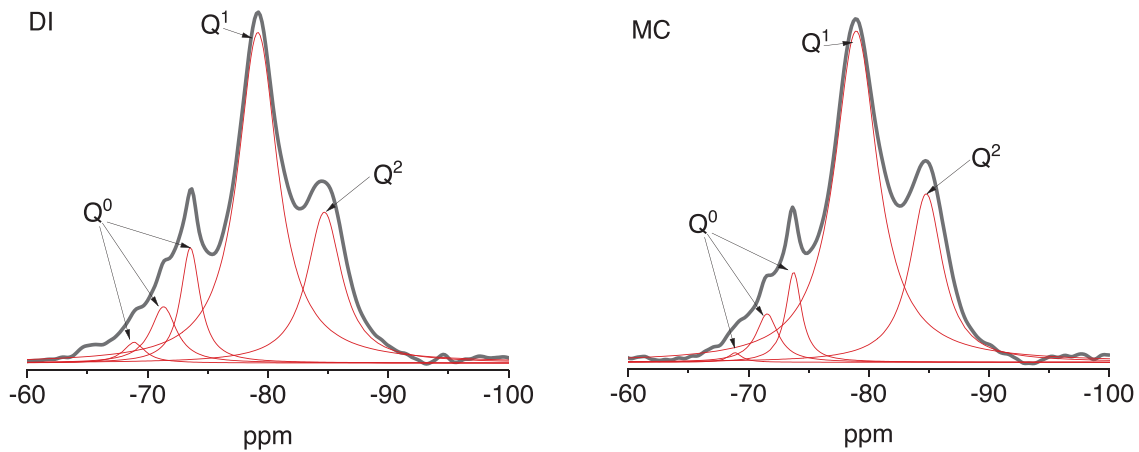

FIGURE 12 ^{29}Si magic-angle spinning (MAS) NMR spectra of hydrated alite mixed with DI water and MC solution at 90 days.

properties of C–S–H when the packing density close to 1 were not affected, the possible degradation mechanism was possibly due to porosity. The incorporation of Mg^{2+} mainly causes the formation of lower packing density C–S–H, which is the main reason for the degradation effect.

4 | CONCLUSIONS

The mechanical properties (modulus and hardness) of alite pastes were studied by mixing Alite with DI water and $MgCl_2$ solutions at both mesoscale and microscale levels. The analysis indicated that at the mesoscale level, the formation of brucite occurred rapidly together with the formation of portlandite that may lead to a faster desaturation of large pores in the pastes and hider the growth of hydration products, leading to a decrease in the packing density

of alite hydration products and subsequent degradation. At the microscale level, using atomistic simulations, Mg^{2+} ions were found to preferably substitute interlayer Ca rather than intralayer Ca in C–S–H. Atomistic simulations also showed a modest swelling to shrinkage behavior at the nanoscale with increasing $Mg^{2+} \rightarrow Ca^{2+}$ substitutions. Overall, the results suggest that the incorporation of Mg^{2+} would not significantly alter the structure and mechanical properties of C–S–H at the nanoscale, clearly demonstrating that Mg inclusion in C–S–H modulus and hardness degradation and overall swelling mainly comes from the formation of Mg-containing phases such as brucite at the mesoscale.

ORCID

Yanjie Sun https://orcid.org/0000-0002-7967-6382

REFERENCES

1. Kummu M, Guillaume JHA, De Moel H, Eisner S, Flörke M, Porkka M, et al. The world's road to water scarcity: shortage and stress in the 20th century and pathways towards sustainability. Sci Rep. 2016;6(1):38495.

2. Miller SA, Horvath A, Monteiro PJM. Impacts of booming concrete production on water resources worldwide. Nat Sustain. 2018;1(1):69–76.

3. Clarke R. Water: the international crisis. 1st ed. Routledge: London; 2013.

4. Witze A. Rare mineral is the key to long–lasting ancient concrete. Nature. 2017. https://doi.org/10.1038/nature.2017.22231

5. Ragab AM, Elgammal MA, Hodhod OA, Ahmed TE. Evaluation of field concrete deterioration under real conditions of seawater attack. Constr Build Mater. 2016;119:130–44.

6. Shang B, Li Y. Application feasibility of HRB400 steel in seawater and marine sand concrete. Corros Mater. 2018;69(10):1478–88.

7. Uthaman S, George R, Vishwakarma V, Harilal M, Philip J. Enhanced seawater corrosion resistance of reinforcement in nanophase modified fly ash concrete. Constr Build Mater. 2019;221:232–43.

8. Wang Z, Zhao XL, Xian G, Wu G, Raman RS, Al-Saadi S, et al. Long-term durability of basalt-and glass-fibre reinforced polymer (BFRP/GFRP) bars in seawater and sea sand concrete environment. Constr Build Mater. 2017;139:467–89.

9. Guo F, Al-Saadi S, Raman RS, Zhao X. Durability of fiber reinforced polymer (FRP) in simulated seawater sea sand concrete (SWSSC) environment. Corros Sci. 2018;141:1–13.

10. Younis A, Ebead U, Suraneni P, Nanni A. Fresh and hardened properties of seawater-mixed concrete. Constr Build Mater. 2018;190:276–86.

11. Khatibmasjedi M, Ramanthan S, Suraneni P, Nanni A. Shrinkage behavior of cementitious mortars mixed with seawater. Adv Civ Eng Mater. 2019;8(2):64–78.

12. Guo M, Hu B, Xing F, Zhou X, Sun M, Sui L, et al. Characterization of the mechanical properties of eco-friendly concrete made with untreated sea sand and seawater based on statistical analysis. Constr Build Mater. 2020;234:117339.

13. Sikora P, Cendrowski K, Abd Elrahman M, Chung SY, Mijowska E, Stephan D. The effects of seawater on the hydration, microstructure and strength development of Portland cement pastes incorporating colloidal silica. Appl Nanosci. 2020;10(8):2627–38.

14. Montanari L, Suraneni P, Tsui-Chang M, Khatibmasjedi M, Ebead U, et al. Hydration, pore solution, and porosity of cementitious pastes made with seawater. J Mater Civ Eng. 2019;31(8):04019154.

15. Li P, Li W, Yu T, Qu F, Tam VW. Investigation on early-age hydration, mechanical properties and microstructure of seawater sea sand cement mortar. Constr Build Mater. 2020;249:118776.

16. Zhang Y, Sun Y, Zheng H, Cai Y, Lam WL, Poon CS. Mechanism of strength evolution of seawater OPC pastes. Adv Struct Eng. 2021;24(6):1256–66.

17. Wang J, Liu E, Li L. Multiscale investigations on hydration mechanisms in seawater OPC paste. Constr Build Mater. 2018;191:891–903.

18. Xiao J, Qiang C, Nanni A, Zhang K. Use of sea-sand and seawater in concrete construction: current status and future opportunities. Constr Build Mater. 2017;155:1101–11.

19. Yaseen SA, Yiseen GA, Poon CS, Li Z. Influence of seawater on the morphological evolution and the microchemistry of hydration products of tricalcium silicates (C_3S). ACS Sustain Chem Eng. 2020;8(42):15875–87.

20. Kaushik SK, Islam S. Suitability of sea water for mixing structural concrete exposed to a marine environment. Cem Concr Compos. 1995;17(3):177–85.

21. Wegian FM. Effect of seawater for mixing and curing on structural concrete. IES J A: Civ Struct Eng. 2010;3(4):235–43.

22. Shi Z, Shui Z, Li Q, Geng H. Combined effect of metakaolin and sea water on performance and microstructures of concrete. Constr Build Mater. 2015;74:57–64.

23. Rocha CAA, Cordeiro GC, Toledo Filho RD. Use of thermal analysis to determine the hydration products of oil well cement pastes containing NaCl and KCl. J Therm Anal Calorim. 2015;122(3):1279–88.

24. Sun Y, Zhang Y, Cai Y, Lam WL, Lu J-X, Shen P, et al. Mechanisms on accelerating hydration of alite mixed with inorganic salts in seawater and characteristics of hydration products. ACS Sustain Chem Eng. 2021;9(31):10479–90.

25. Sun Y, Yaphary YL, Poon CS. Experimental and mesoscale simulation studies of micro-mechanical properties of alite mixed with NaCl solutions. Cem Concr Res. 2022;159:106890.

26. Sun Y, Lu JX, Shen P, Poon CS. Hydration kinetics and microstructure evolution of NaCl-mixed tricalcium silicate pastes. Cem Concr Res. 2022;161:106934.

27. Sun Y, Lu JX, Poon CS. Strength degradation of seawater-mixed alite pastes: an explanation from statistical nanoindentation perspective. Cem Concr Res. 2022;152:106669.

28. Fernandez L, Alonso C, Hidalgo A, Andrade C. The role of magnesium during the hydration of C_3S and CSH formation. Scanning electron microscopy and mid-infrared studies. Adv Cem Res. 2005;17(1):9–21.

29. Fernandez L, Alonso C, Andrade C, Hidalgo A. The interaction of magnesium in hydration of C_3S and CSH formation using ^{29}Si MAS-NMR. J Mater Sci. 2008;43(17):5772–83.

30. Liu X, Feng P, Yu X, Shen X, Geng G, Lothenbach B. The physiochemical alterations of calcium silicate hydrate (C–S–H) under magnesium attack. Cem Concr Res. 2022;160 106901.

31. Miron GD, Kulik DA, Yan Y, Tits J, Lothenbach B. Extensions of CASH+ thermodynamic solid solution model for the uptake of alkali metals and alkaline earth metals in C–S–H. Cem Concr Res. 2022;152:106667.

32. Hu C and Li Z. A review on the mechanical properties of cement-based materials measured by nanoindentation. Constr Build Mater. 2015;90:80–90.

33. Velez K, Maximilien S, Damidot D, Fantozzi G, Sorrentino F. Determination by nanoindentation of elastic modulus and hardness of pure constituents of Portland cement clinker. Cem Concr Res. 2001;31(4):555–61.

34. Pellenq RJM, Kushima A, Shahsavari R, Van Vliet KJ, Buehler MJ, Yip S, et al. A realistic molecular model of cement hydrates. Proc Natl Acad Sci. 2009;106(38):16102.

35. Abdolhosseini Qomi MJ, Ulm FJ, Pellenq RJM. Evidence on the dual nature of aluminum in the calcium–silicate–hydrates based on atomistic simulations. J Am Ceram Soc. 2012;95(3):1128–37.

36. Li XR, Ouzia A, Scrivener K. Laboratory synthesis of C_3S on the kilogram scale. Cem Concr Res. 2018;108:201–7.

37. Scrivener K, Snellings R, Lothenbach B. A practical guide to microstructural analysis of cementitious materials. CRC Press; 2018.

38. Bergold ST, Goetz-Neunhoeffer F, Neubauer J. Quantitative analysis of C–S–H in hydrating alite pastes by in-situ XRD. Cem Concr Res. 2013;53:119–26.

39. Luo Z, Li W, Gan Y, Mendu K, Shah SP. Applying grid nanoindentation and maximum likelihood estimation for N–A–S–H gel in geopolymer paste: investigation and discussion. Cem Concr Res. 2020;135 106112.

40. Ulm FJ, Vandamme M, Bobko C, Alberto Ortega J, Tai K, Ortiz C. Statistical indentation techniques for hydrated nanocomposites: concrete, bone, and shale. J Am Ceram Soc. 2007;90(9):2677–92.

41. Vandamme M, Ulm F-J, Fonollosa P. Nanogranular packing of C–S–H at substochiometric conditions. Cem Concr Res. 2010;40(1):14–26.

42. Labbez C, Jönsson B, Pochard I, Nonat A, Cabane B. Surface charge density and electrokinetic potential of highly charged minerals: experiments and Monte Carlo simulations on calcium silicate hydrate. J Phys Chem B. 2006;110(18):9219–30.

43. Nicholson W, Nicholson D, Parsonage NG. Computer simulation and the statistical mechanics of adsorption. Academic Press; 1982.

44. Abdolhosseini Qomi MJ, Krakowiak KJ, Bauchy M, Stewart KL, Shahsavari R, Jagannathan D, et al. Combinatorial molecular optimization of cement hydrates. Nat Commun. 2014;5(1):4960.

45. Qomi MJA, Bauchy M, Ulm FJ, Pellenq RJM. Anomalous composition-dependent dynamics of nanoconfined water in the interlayer of disordered calcium-silicates. J Chem Phys. 2014;140(5):054515.

46. Abdolhosseini Qomi MJ, Ulm FJ, Pellenq RJM. Physical origins of thermal properties of cement paste. Phys Rev Appl. 2015;3(6):064010.

47. Dezerald L, Kohanoff JJ, Correa AA, Caro A, Pellenq RJM, Ulm FJ, et al. Cement as a waste form for nuclear fission products: the case of 90Sr and its daughters. Environ Sci Technol. 2015;49(22):13676–83.

48. Gale JD, Rohl AL. The general utility lattice program (GULP). Mol Simul. 2003;29(5):291–341.

49. Gale JD. Empirical potential derivation for ionic materials. Philos Mag B. 1996;73(1):3–19.

50. Auzende AL, Pellenq RJM, Devouard B, Baronnet A, Grauby O. Atomistic calculations of structural and elastic properties of serpentine minerals: the case of lizardite. Phys Chem Miner. 2006;33(4):266–75.

51. Chen JJ, Sorelli L, Vandamme M, Ulm FJ, Chanvillard G. A coupled nanoindentation/SEM–EDS study on low water/cement ratio Portland cement paste: evidence for C–S–H/Ca(OH)$_2$ nanocomposites. J Am Ceram Soc. 2010;93(5):1484–93.

52. Zhang M, Zunino F, Yang L, Wang F, Scrivener K. Understanding the negative effects of alkalis on long-term strength of Portland cement. Cem Concr Res. 2023;174 107348.

53. Tao Y, Gao Y, Sun Y, Pellenq RJM, Poon CS. C–S–H decalcification in seawater: the view from the nanoscale. Cem Concr Res. 2024;175:107385.

54. Pellenq RJM, Lequeux N, van Damme H. Engineering the bonding scheme in C–S–H: the iono-covalent framework. Cem Concr Res. 2008;38(2):159–74.

55. Cai Y, Tao Y, Xuan D, Zhu X, Poon CS. Effects of seawater on the formation and mechanical properties of Friedel's salt associated with tricalcium aluminate. Cem Concr Res. 2023;174: 107340.

56. Cai Y, Tao Y, Xuan D, Sun Y, Poon CS. Effect of seawater on the morphology, structure, and properties of synthetic ettringite. Cem Concr Res. 2023;163:107034.

57. Bernard E, Lothenbach B, Cau-Dit-Coumes C, Chlique C, Dauzères A, et al. Magnesium and calcium silicate hydrates, Part I: Investigation of the possible magnesium incorporation in calcium silicate hydrate (C–S–H) and of the calcium in magnesium silicate hydrate (M–S–H). Appl Geochem. 2018;89:229–42.

58. Bell GMM, Bensted J, Glasser FP, Lachowski EE, Roberts DR, Taylor MJ. Study of calcium silicate hydrates by solid state high resolution ^{29}Si nuclear magnetic resonance. Adv Cem Res. 1990;3(9):23–27.

59. Sánchez-Herrero MJ, Fernández-Jiménez A, Palomo A. C_3S and C_2S hydration in the presence of Na_2CO_3 and Na_2SO_4. J Am Ceram Soc. 2017;100(7):3188–98.

60. Zhang L, Cheng X, Hou D, Guo S. Hydration for the Alite mineral: morphology evolution, reaction mechanism and the compositional influences. Constr Build Mater. 2017;155:413–26.

61. Beaudoin JJ, Raki L, Alizadeh R. A ^{29}Si MAS NMR study of modified C–S–H nanostructures. Cem Concr Compos. 2009;31(8):585–90.

62. Richardson IG. Tobermorite/jennite- and tobermorite/calcium hydroxide-based models for the structure of C–S–H: applicability to hardened pastes of tricalcium silicate, β-dicalcium silicate, Portland cement, and blends of Portland cement with blast-furnace slag, metakaolin, or silica fume. Cem Concr Res. 2004;34(9):1733–77.

SUPPORTING INFORMATION

Additional supporting information can be found online in the Supporting Information section at the end of this article.